Title
Axisymmetric simulations of libration-driven fluid dynamics in a spherical shell geometry

Journal
Physics of Fluids, 22(8)

ISSN
1070-6631

Authors
Calkins, Michael A
Noir, Jérôme
Eldredge, Jeff D
et al.

Publication Date
2010-08-01

DOI
10.1063/1.3475817

Peer reviewed

Axisymmetric simulations of libration-driven fluid dynamics in a spherical shell geometry

Michael A. Calkins,[1,a)] Jérôme Noir,[2] Jeff D. Eldredge,[1] and Jonathan M. Aurnou[2]
[1]*Department of Mechanical and Aerospace Engineering, University of California, Los Angeles, California 90095, USA*
[2]*Department of Earth and Space Sciences, University of California, Los Angeles, California 90095, USA*

(Received 6 April 2010; accepted 29 June 2010; published online 26 August 2010)

We report on axisymmetric numerical simulations of rapidly rotating spherical shells in which the axial rotation rate of the outer shell is modulated in time. This allows us to model planetary bodies undergoing forced longitudinal libration. In this study we systematically vary the Ekman number, $10^{-7} \leq E \leq 10^{-4}$, which characterizes the ratio of viscous to Coriolis forces in the fluid, and the libration amplitude, $\Delta\phi$. For libration amplitudes above a certain threshold, Taylor–Görtler vortices form near the outer librating boundary, in agreement with the previous laboratory experiments of Noir *et al.* [Phys. Earth Planet. Inter. **173**, 141 (2009)]. At the lowest Ekman numbers investigated, we find that the instabilities remain spatially localized at onset in the equatorial region. In addition, nonzero time-averaged azimuthal (zonal) velocities are observed for all parameters studied. The zonal flow is characterized by predominantly retrograde flow in the interior, with a stronger prograde jet in the outer equatorial region. The magnitude of the zonal flow scales as the square of the librational forcing, ϵ^2, where $\epsilon = \Delta\phi f$ and f is the dimensionless libration frequency defined as the ratio between the libration frequency and the mean angular rotation rate. In addition, the zonal flow is primarily independent of the Ekman number, implying that the zonal flow does not depend on the viscosity of the fluid. The simulations show that the zonal flow is driven by nonlinearities in the Ekman boundary layer; it is not driven by Taylor–Görtler vortices or by inertial waves in the fluid interior. Application of our results suggests that many librating bodies in the solar system are above the onset for centrifugal instabilities, with values up to ~30 times supercritical. However, the spatial localization of the instabilities at onset in our simulations suggests that their effects are limited on the global dynamics of librating bodies. We find that the zonal flows driven by libration in axisymmetric spherical shells are unlikely to produce significant planetary magnetic fields, but will likely generate nonzero mean torques on the bounding surfaces. © *2010 American Institute of Physics*. [doi:10.1063/1.3475817]

I. INTRODUCTION

Many planetary bodies in the solar system have a time-periodic axial rotation rate, known as longitudinal libration.[1] This motion is the result of periodically reversing gravitational torques acting on asymmetries in mass of the planet. Some of the bodies undergoing longitudinal libration, such as Mercury and the Galilean satellites, are inferred to possess liquid metal cores or subsurface liquid water oceans (e.g., Refs. 2 and 3). It is likely that exchanges of angular momentum between the outer librating shell and the interior fluid volume of these bodies is presently occurring. The exchange of angular momentum can occur through viscous, gravitational, electromagnetic, and topographic coupling. Viscous coupling is perhaps the simplest mechanism to model from both a numerical and laboratory standpoint and so provides a useful starting point from which to begin an examination on the fluid dynamical effects of libration. It is also likely to be the weakest of the coupling mechanisms,[4] thus providing a useful lower bound on librationally driven flow velocities. For these reasons, the current study focuses entirely on the viscously excited flows generated by libration.

We characterize the oscillatory motion of a librating body by a single (angular) libration frequency, $\omega_L = 2\pi/P_L$, where P_L is the libration period. In general, the librational motion of a given planetary body is composed of several different periods, where the libration period with the largest amplitude corresponds to the orbital period (e.g., see Refs. 1 and 3). Thus, our results can be used to understand a particular planet's response to that period which is characterized by the largest amplitude.

The range of libration frequencies present throughout the universe is likely to be broad. When a librating body is in synchronous rotation, its rotation period is equal to its orbital period around the primary.[1] In such cases, the dimensionless libration frequency, $f = \omega_L/\Omega_o$, where Ω_o is the mean rotation rate of the librating body, is unity. This value is applicable, for example, to the Earth's moon and the Galilean satellites.[1] Mercury, however, completes three rotations for every two orbits around the sun, resulting in $f = 2/3$. Future space missions and telescopic observations will likely yield more diverse libration frequencies (e.g., Ref. 5). We focus primarily

a)Author to whom correspondence should be addressed. Electronic mail: mcalkins@ucla.edu.

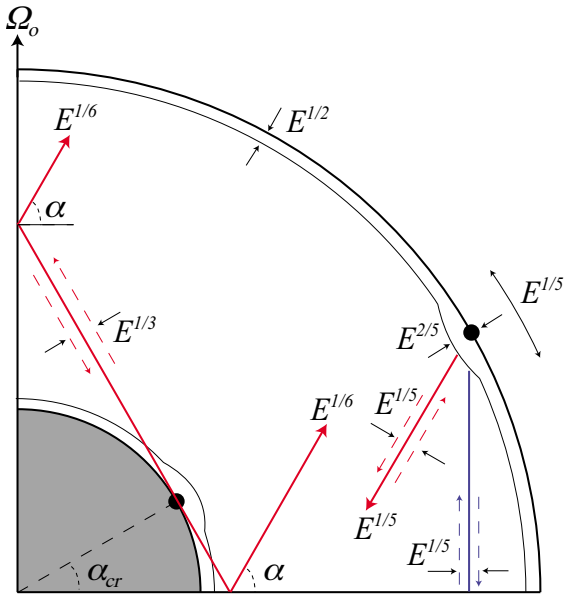

FIG. 1. (Color online) Schematic showing velocity and length scalings for internal shear and boundary layers in a rapidly rotating spherical shell (modified from Ref. 9). Thin, solid (black) arrows denote layer thicknesses. Dots (black) on the inner and outer boundary represent the critical latitude. The solid, oblique (red) lines represent oscillatory shear layers resulting from the velocity singularity at the critical latitude. The steady, geostrophic shear layer is denoted by the vertical, solid (blue) line emanating from the critical latitude on the outer boundary. The scalings for the Ekman boundary layer present on the inner sphere are identical to those on the outer sphere.

on the frequency $f=1$, which is characteristic of most librating bodies.

In a rotating spherical shell containing a homogenous fluid, the motion of the librating boundary is transmitted viscously to the interior fluid through the thin Ekman boundary layer that is present along the outer librating surface. The flux of mass into or out of the Ekman layer induces oscillations in the fluid volume in the form of inertial modes.[6] Inertial modes are the natural modes of oscillation for a rotating fluid body and propagate throughout the fluid interior along conical characteristic surfaces.[7,8] We shall refer to the disturbances propagating along these paths as inertial waves. As shown in Fig. 1, we define the angle between the characteristic surfaces and the equatorial plane as α. Assuming linear dynamics, this angle is solely dependent on the forcing frequency f and is given by

$$f = 2 \cos \alpha. \tag{1}$$

Inertial waves exist only in the finite frequency band $|f| \leq 2$. Steady (geostrophic) motion is characterized by $f=0$ and, therefore, by characteristic surfaces that are parallel to the rotation axis, giving $\alpha=\pi/2$ rad. For $f=1$ we have $\alpha=\pi/3$ rad. Finally, for $f=2$, the characteristic surfaces are perpendicular to the rotation axis, $\alpha=0$. For fully nonlinear systems, as investigated here, harmonics and subharmonics of f can also be generated.

The physical structure and amplitude of inertial waves are dependent on the ratio of viscous forces to the Coriolis force, denoted by the Ekman number, $E=\nu/(\Omega_o r_o^2)$, where ν is the kinematic viscosity of the fluid and r_o is the radius of the outer shell. The magnitude of the mass flux flowing through the Ekman layer typically scales as $E^{1/2}$. This behavior changes at locations along the boundaries where the reflected energy of an incident inertial wave is tangent to that boundary. In a spherical system, this location is known as the critical latitude, α_{cr}, and is given by the relation[6]

$$f = 2 \sin \alpha_{cr}. \tag{2}$$

Therefore, $\alpha+\alpha_{cr}=\pi/2$ rad. At the critical latitude on both the outer and inner spherical shell boundaries, there is a local increase in the thickness of the Ekman layer from $E^{1/2}$ to $E^{2/5}$.[10] Typically, the mass flux in and out of the Ekman layer, referred to as Ekman pumping, scales as $E^{1/2}$. However, at the critical latitude on the outer boundary, the mass flux at the critical latitude increases, scaling as $E^{1/5}$ over an angular distance of $E^{1/5}$.[11] Furthermore, at the critical latitude on the inner boundary, the anomalous Ekman pumping generates a shear layer tangent to the local spherical shell surface. This shear layer is of width $E^{1/3}$ and is characterized by tangential velocities that scale as $E^{1/6}$.[9] The properties of the internal shear layers and the boundary layers occurring in a rotating spherical shell are summarized in Fig. 1.

Previous laboratory[12,13] and numerical[14] work has employed longitudinal libration as a convenient mechanism for exciting inertial waves in rotating spheres and spherical shells due to the properties stated above. Tilgner[14] investigated the attractors associated with inertial waves in a spherical shell. Aldridge[12] and Aldridge and Toomre[13] tested theoretically predicted inertial mode resonance frequencies (e.g., see Ref. 6) and determined the associated viscous decay rates. Aldridge[12] also found that when the libration amplitude was above a certain threshold, Taylor–Görtler vortexlike instabilities developed along the outer librating shell.

The recent experimental investigation of Noir *et al.*[15] (hereafter referred to as N09) expanded the work of Aldridge by covering a broad range in libration frequency, amplitude, Ekman number, and inner core radius. The authors determined the stability boundaries for the onset of Taylor–Görtler vortex formation and their subsequent breakdown into boundary layer turbulence. They also observed little dependence of the flow regimes on the presence and size of an inner sphere. The results suggest many librating bodies are within the unstable or turbulent regime. However, as the laboratory experiments were limited to $E \geq 10^{-5}$, additional work is necessary to confirm that their results can be realistically extrapolated to the low Ekman numbers ($E \lesssim 10^{-12}$) that are characteristic of planets.

It is of general interest in rotating fluid mechanics to understand the conditions under which mean azimuthal (zonal) flows can be generated (e.g., see Refs. 16–18). It has been shown experimentally[19] and analytically[20] that nonlinearities in the Ekman boundary layer can drive large-scale zonal flows in librating systems. Busse[21] first studied the zonal flow produced by local nonlinearities in the Ekman boundary layer at the critical latitude. He showed that these nonlinearities will drive a strong radial shear along a geostrophic cylinder coaxial with the rotation axis at the radius $s_{cr}=r_o \cos \alpha_{cr}$. We refer to this shear structure as the geo-

strophic shear layer (see Fig. 1). Thus far, studies predict a divergent radial shear along s_{cr} as $E \to 0$.[11,21]

In the current study we employ axially and equatorially symmetric, fully nonlinear numerical simulations to investigate under what conditions forced longitudinal libration generates Taylor–Görtler vortices and mean zonal flows at Ekman numbers $10^{-7} \leq E \lesssim 10^{-4}$. The lowest Ekman numbers investigated here are over two orders of magnitude smaller than in comparable studies.[12,13,19] In Sec. II we outline the numerical methods used in our simulations, in Sec. III we present our results, and in Sec. IV we discuss our results and their planetary implications.

II. METHODOLOGY

The physical system we investigate consists of a homogeneous, Newtonian fluid contained in a rapidly rotating spherical shell with outer radius, r_o, and inner radius, r_i. In the simulations reported here we use a geometrically thick spherical shell of radius ratio $\eta = r_i/r_o = 0.35$. The rotation rate of the outer solid, spherical boundary is modulated in time, t, with angular frequency ω_L and libration amplitude, $\Delta\phi$, and is given by

$$\Omega(t) = \Omega_o + \Delta\phi\omega_L \sin(\omega_L t). \tag{3}$$

The inner solid sphere rotates at the constant rate Ω_o.

For small libration amplitudes, the librational forcing drives axisymmetric and equatorially symmetric flow in the spherical shell. Two-dimensional numerical simulations can thus be performed, greatly reducing computational expense and allowing for lower Ekman numbers than would be accessible in fully three-dimensional models. The difficulty associated with low Ekman number simulations is due to the small length and time scales that must be used to avoid numerical instabilities and to maintain numerical accuracy. For instance, the Ekman boundary layers scale as $E^{1/2}$, which requires increasingly high spatial resolution as the Ekman number is reduced. Furthermore, at least 100 time steps per rotation are required to resolve the fastest inertial waves.

We solve the fully nonlinear Navier–Stokes equations for an incompressible fluid. This is done using a vorticity-stream function formulation in the meridional plane of a spherical coordinate system (r, θ, ϕ), which rotates with rate Ω_o, where the radial, colatitudinal, and azimuthal velocity components are given by u, v, and w, respectively. The vorticity-stream function method allows the pressure to be eliminated from the governing equations and mass to be exactly conserved. A schematic of the flow domain is shown in Fig. 2.

The azimuthal vorticity, ζ, is given by

$$\zeta = \frac{1}{r}\frac{\partial}{\partial r}(rv) - \frac{1}{r}\frac{\partial u}{\partial \theta}. \tag{4}$$

Physically, the azimuthal vorticity describes the rotational direction of individual fluid elements in the meridional plane; positive vorticity corresponds to locally clockwise motion and negative vorticity corresponds to counterclockwise motion. The meridional stream function, ψ, is defined by the relations

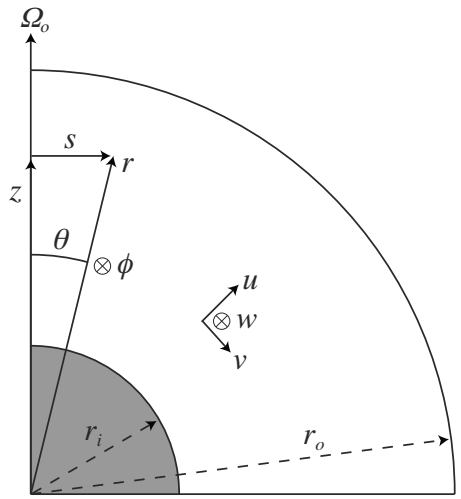

FIG. 2. Drawing of the flow domain and spherical coordinate system used in the numerical simulations. The spherical coordinate system used is (r, θ, ϕ) with corresponding velocities (u, v, w). The inner and outer radii are r_i and r_o, respectively. The cylindrical radius is given by $s = r \sin\theta$ and the cylindrical coordinate z is given by $z = r\cos\theta$.

$$u = \frac{1}{r^2 \sin\theta}\frac{\partial \psi}{\partial \theta}, \tag{5}$$

$$v = -\frac{1}{r \sin\theta}\frac{\partial \psi}{\partial r}. \tag{6}$$

Note that the meridional stream function formulation, by definition, requires mass to be conserved. Combining Eq. (4) with Eqs. (5) and (6) we have the following equation relating the stream function to the azimuthal vorticity:

$$\zeta = -\frac{1}{r \sin\theta}\frac{\partial^2 \psi}{\partial r^2} - \frac{1}{r^3}\frac{\partial}{\partial \theta}\left(\frac{1}{\sin\theta}\frac{\partial \psi}{\partial \theta}\right). \tag{7}$$

Using the outer radius, r_o, as the basic length scale, and the inverse of the mean rotation rate, Ω_o^{-1}, as the basic time scale, the nondimensional equations for the azimuthal velocity and azimuthal vorticity are written, respectively, as

$$\frac{\partial w}{\partial t} + u\frac{\partial w}{\partial r} + \frac{v}{r}\frac{\partial w}{\partial \theta} + w\left(\frac{u}{r} + \cot\theta\frac{v}{r}\right) + 2u\sin\theta + 2v\cos\theta = E\nabla^2 w \tag{8}$$

and

$$\frac{\partial \zeta}{\partial t} + u\frac{\partial \zeta}{\partial r} + \frac{v}{r}\frac{\partial \zeta}{\partial \theta} + w\left(\frac{1}{r^2 \sin\theta}\frac{\partial}{\partial \theta}(w\sin\theta) - \frac{\cot\theta}{r^2}\frac{\partial}{\partial r}(rw)\right) - \zeta\left(\frac{u}{r} + \frac{v}{r}\cot\theta\right) = \left(\frac{1}{r\sin\theta}\frac{\partial}{\partial \theta}(w\sin\theta) + 2\cos\theta\right)\frac{\partial w}{\partial r} + \left(\frac{1}{r}\frac{\partial}{\partial r}(rw) - 2\sin\theta\right)\frac{1}{r}\frac{\partial w}{\partial \theta} + E\nabla^2\zeta, \tag{9}$$

where we use the notation

$$\nabla^2(\cdot) = \frac{1}{r^2}\frac{\partial}{\partial r}\left[r^2\frac{\partial(\cdot)}{\partial r}\right] + \frac{1}{r^2}\frac{\partial}{\partial\theta}\left\{\frac{1}{\sin\theta}\frac{\partial}{\partial\theta}[(\cdot)\sin\theta]\right\}. \tag{10}$$

No-slip boundary conditions are employed along the inner and outer spherical surfaces,

$$w(1,\theta,t) = \epsilon\sin\theta\sin(ft), \tag{11}$$

$$w(\eta,\theta,t) = 0, \tag{12}$$

$$\frac{\partial\psi}{\partial r}(\eta,\theta) = \frac{\partial\psi}{\partial r}(1,\theta) = 0, \tag{13}$$

where

$$\epsilon = \Delta\phi f \tag{14}$$

is the librational forcing. Stress free boundary conditions are applied along the rotation axis and equatorial plane

$$\zeta(r,0) = \zeta(r,\pi/2) = 0, \tag{15}$$

and zero mass flux is enforced along the symmetry planes and solid boundaries

$$\psi(\eta,\theta) = \psi(1,\theta) = \psi(r,0) = \psi(r,\pi/2) = 0. \tag{16}$$

The colatitudinal components of the diffusive terms present in Eqs. (7)–(9) can be simplified by introducing the following substitutions:

$$A = rw\sin\theta, \quad B = -r\zeta\sin\theta. \tag{17}$$

Note that the quantity, A, is the local axial angular momentum of a fluid parcel. The variables are then expanded in the form

$$A(r,\theta,t) = \sum_{\substack{n=1\\ n\ \text{odd}}}^{L} A_n(r,t)\sin\theta P_n^1(\theta), \tag{18}$$

$$B(r,\theta,t) = \sum_{\substack{n=1\\ n\ \text{even}}}^{L} B_n(r,t)\sin\theta P_n^1(\theta), \tag{19}$$

$$\psi(r,\theta,t) = \sum_{\substack{n=1\\ n\ \text{even}}}^{L} \psi_n(r,t)\sin\theta P_n^1(\theta), \tag{20}$$

where P_n^1 are the first associated Legendre functions and L is the maximum degree Legendre function used. The symmetry of the problem allows us to only consider the odd degree Legendre functions for A and the even degree functions for B and ψ. Expansions of this type have been used, for example, by Dennis and Walker.[22] The resulting Legendre–Galerkin equations are discretized in radius using a second-order accurate finite difference scheme. A second-order accurate Adams–Bashforth/backward differentiation scheme is employed to advance the solution in time.[23] The influence matrix method is used to account for the lack of boundary conditions for the vorticity along the inner and outer spherical boundaries. This method exploits the linearity of the time-discretized equations by using a linear combination of the vorticity and stream function such that the boundary conditions on the stream function are satisfied. Further details of this method can be found in the text by Peyret.[23] We use associated Legendre functions up to degree $L=1800$ and $N=1301$ radial grid points for the most demanding calculations. The grids used for the results presented in this study are shown in Table I. The nondimensional time-step sizes ranged from 10^{-2} to 10^{-3}. The majority of the simulations used Gauss–Lobatto (Chebyshev) points to increase the radial resolution near the inner and outer solid boundaries in order to resolve the Ekman layers (e.g., see Ref. 23). For our lowest Ekman number cases, the radial distribution function presented by Tilgner[14] is used, which better resolves the Ekman layer. The code has been benchmarked with a three-dimensional libration code developed by R. Laguerre (personal communication) and with previous axisymmetric spherical Taylor–Couette studies (e.g., Refs. 24 and 25).

TABLE I. Parameters used for libration simulations. $\Delta\phi_{cr}$ and m_{cr} are the critical libration amplitude in radians and the critical latitudinal wavenumber, respectively. Runs with no entries (⋯) for $\Delta\phi_{cr}$ and m_{cr} were centrifugally stable.

E	f	L	N	$\Delta\phi_{cr}$	m_{cr}
$10^{-4.2}$	1	600	401	0.34	12
$10^{-4.4}$	1	640	421	0.25	23
$10^{-4.6}$	1	640	441	0.21	26
$10^{-4.8}$	1	660	441	0.18	44
10^{-5}	1	800	501	0.15	49
10^{-5}	2.2	800	501	⋯	⋯
$10^{-5.2}$	1	900	601	0.128	55
$10^{-5.4}$	1	900	601	0.10	78
$10^{-5.6}$	1	1140	721	0.078	101
$10^{-5.8}$	1	1500	841	0.063	126
10^{-6}	1	1800	901	0.05	153
$10^{-6.5}$	1	900	1301	⋯	⋯
10^{-7}	1	1200	801	⋯	⋯

III. RESULTS

A. Inertial waves

When the librational forcing is small (i.e., $\epsilon \ll 1$), the fluid volume is dominated by inertial waves. Figure 3 shows stream function contours at the instant when the outer shell is at the maximum retrograde position for an Ekman number of $10^{-6.5}$, $\epsilon = 10^{-3}$, and $f=1$. We see that the flow structure is dominated by the oblique shear layers that are spawned from the critical latitude at the outer boundary (denoted by the tick marks in the figure). These disturbances propagate along the characteristic surfaces. The basic structure of the time dependent flow shown in Fig. 3 is also present at higher libration amplitudes. For detailed discussions concerning inertial waves in spheres and spherical shells, see the works of Aldridge and Toomre,[13] Rieutord,[26] Rieutord and Valdetarro,[27] and Tilgner.[14]

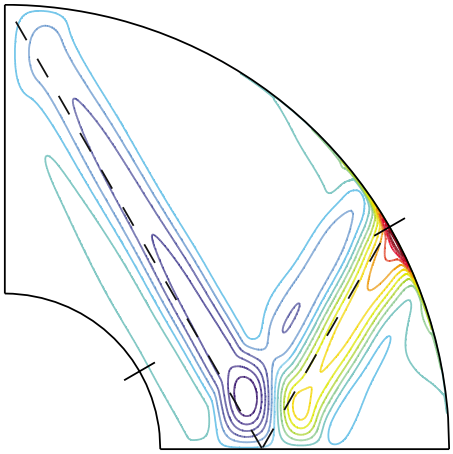

FIG. 3. (Color online) Stream function contours for $E=10^{-6.5}$, $\epsilon=10^{-3}$, and $f=1$ at the instant when the outer boundary is at the maximum retrograde position. Tick marks show the location of the critical latitude on the inner and outer boundaries; oblique dashed lines show the characteristic surfaces of the inertial waves.

B. Onset behavior of centrifugal instabilities

Our numerical simulations show that, for fixed Ekman number E and libration frequency f, there exists a critical libration amplitude, $\Delta\phi_{cr}$, at which the basic librationally driven flow becomes unstable. Figures 4(a) and 4(b) show the structure of the instabilities at the instant when the outer sphere is at the maximum retrograde position for two different Ekman numbers, $E=10^{-4.2}$ and 10^{-5}. The instabilities consist of counter-rotating Taylor–Görtler vortices that are similar to those that occur in both spherical (e.g., Refs. 24, 28, and 29) and cylindrical Taylor–Couette flows.[30] Taylor–Görtler vortices can be defined as fluid instabilities resulting from an adverse angular momentum gradient (e.g., see Refs. 31 and 32); their presence is typified by closed stream function contours [as shown in Figs. 4(e) and 4(f)]. The vortices remain spatially localized within the fluid volume; they are always observed to occur in the equatorial region adjacent to the outer librating shell where the radial shear is largest.

A libration cycle can be decomposed into a prograde and retrograde phase; a prograde phase is defined as that part of the cycle when the outer boundary is rotating in the same direction as the background rotation, whereas the retrograde phase occurs when the outer boundary rotates in the opposite direction as the background rotation. The instabilities grow during the retrograde phase of the libration cycle, when adverse radial gradients in angular momentum are present; this is consistent with Rayleigh's circulation criterion for centrifugal instabilities.[31] Figures 4(e) and 4(f) show the meridional stream function averaged over ten libration cycles. The strong time-averaged signature of the vortices demonstrates that they form at nearly the same location over each libration cycle.

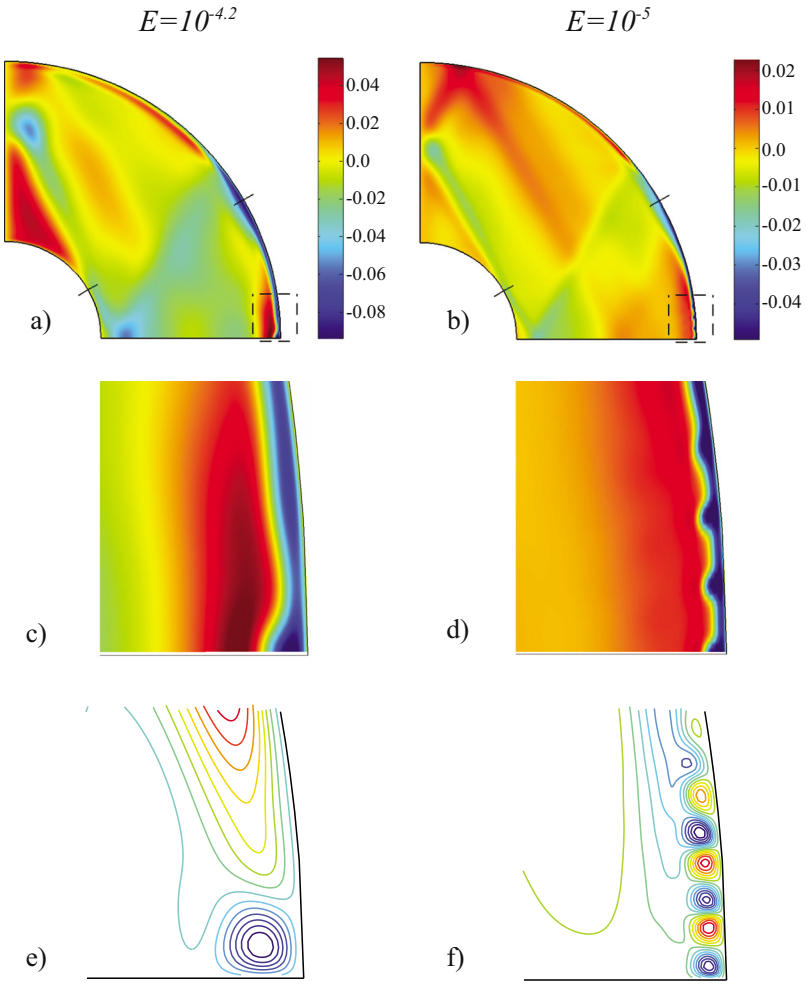

FIG. 4. (Color online) Azimuthal velocity at the moment when the outer shell is at the maximum retrograde position for centrifugally unstable cases: (a) $E=10^{-4.2}$, $\epsilon=0.33$ and (b) $E=10^{-5}$, $\epsilon=0.15$. (c) and (d) show close-up view of instabilities in equatorial region for (a) and (b), respectively. [(e) and (f)] Time-averaged stream function contours for cases shown in (c) and (d). The boxes shown in (a) and (b) denote the regions magnified in (c)–(f). All cases shown are for $f=1$.

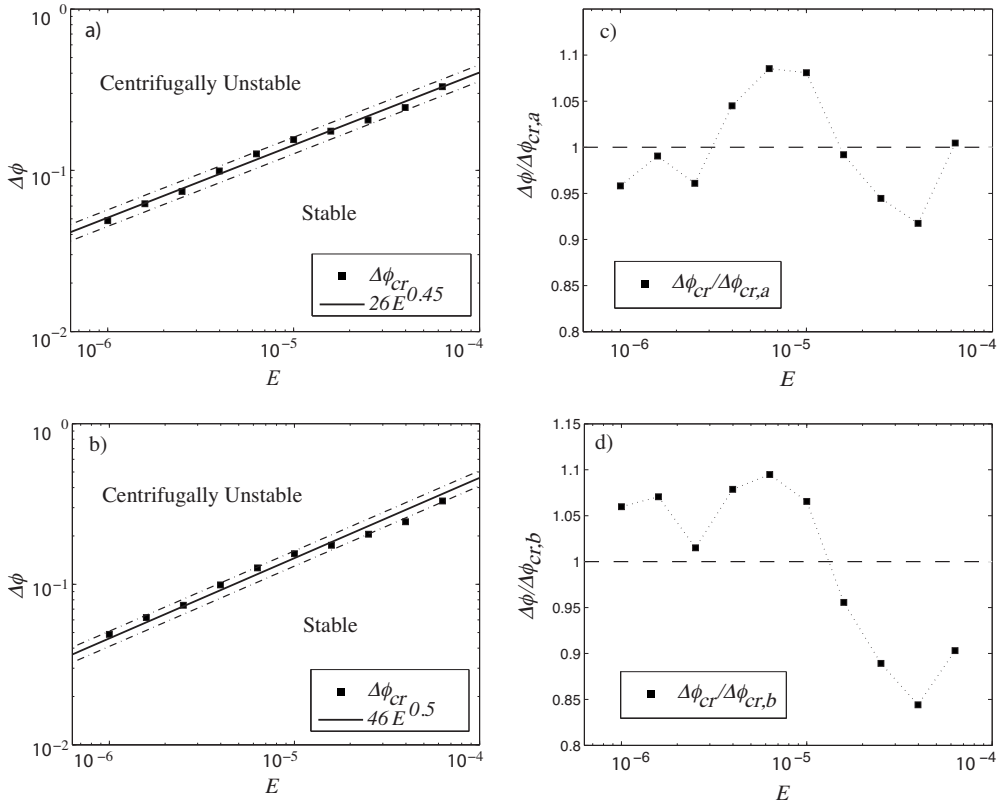

FIG. 5. (a) Stability diagram for the onset of Taylor–Görtler vortices in libration with a best fit line to the data obtained in the current study. (b) Stability diagram for the onset of Taylor–Görtler vortices in libration with the constant boundary layer Reynolds number, $\mathrm{Re}_{\mathrm{BL}}$, scaling proposed by N09. (c) Critical libration amplitude normalized by the best fit line $\Delta\phi_{\mathrm{cr},a}=26E^{0.45}$. (d) Critical libration amplitude normalized by the best fit line $\Delta\phi_{\mathrm{cr},b}=46E^{0.5}$.

To better understand the parameters for which Taylor–Görtler vortices develop in librating systems, we have performed a suite of simulations over the Ekman range of $10^{-6}\leq E\leq 10^{-4.2}$ with a resolution of $\delta E=10^{0.2}$. The process of determining the stability of the basic flow consisted of beginning at a particular libration amplitude and gradually increasing the value until the instabilities were observed. The observations of the instabilities were determined via two methods: (i) visually from the data represented in physical space and (ii) spectrally from the Legendre spectra of the various flow variables. The instabilities were typically first observed visually and their presence was then confirmed using the Legendre spectra. Simulations were then repeated at slightly smaller libration amplitudes to identify the stability boundary.

The results for the onset of the centrifugal instabilities are shown in Fig. 5. The critical libration amplitude, $\Delta\phi_{\mathrm{cr}}$, is determined by linearly interpolating between the largest stable $\Delta\phi$ and the smallest unstable $\Delta\phi$ at each Ekman number. Figures 5(a) and 5(b) show $\Delta\phi_{\mathrm{cr}}$ as a function of E. In Fig. 5(a) we plot the best fit for our data (solid line), which is given by

$$\Delta\phi_{\mathrm{cr},a}=(26\pm 3)E^{0.45\pm 0.01}. \tag{21}$$

Figure 5(b) shows the scaling law given in N09, $\Delta\phi_{\mathrm{cr},b}=(46\pm 4)E^{1/2}$, where the prefactor of 46 was determined using data from the current study. The dotted-dashed lines shown in Figs. 5(a) and 5(b) represent the standard deviation of the prefactors for $\Delta\phi_{\mathrm{cr},a}$ and $\Delta\phi_{\mathrm{cr},b}$.

The scaling law for the onset of the Taylor–Görtler vortices given in N09 is based on a boundary layer Reynolds number, defined as $\mathrm{Re}_{\mathrm{BL}}=\epsilon E^{-1/2}$, where the length scale is based on the thickness of the Ekman layer and the velocity scale is the azimuthal velocity of the outer boundary at the equator. N09 found the critical boundary layer Reynolds number to be $\mathrm{Re}_{\mathrm{BL,cr}}\approx 20$ for $10^{-5}\lesssim E\lesssim 10^{-4}$. Rewriting the expression for the boundary layer Reynolds number in terms of a critical libration amplitude we have

$$\Delta\phi_{\mathrm{cr}}=\mathrm{Re}_{BL,cr}f^{-1}E^{1/2}. \tag{22}$$

This is the scaling relationship shown in Fig. 5(b), where we determined the critical boundary layer Reynolds number for the current study to be $\mathrm{Re}_{\mathrm{BL,cr}}\approx 46$. This value is somewhat larger than that determined by N09; one possible explanation for this discrepancy is the inherent higher noise level present in their experimental apparatus. Nevertheless, due to the uncertainty in our determination of $\Delta\phi_{\mathrm{cr}}$, our results are consistent with the $\Delta\phi_{\mathrm{cr}}\sim E^{1/2}$ scaling presented by N09.

Also apparent from the numerical data shown in Figs. 5(a) and 5(b) is the wavy character of the stability boundary. To highlight this behavior, Figs. 5(c) and 5(d) show the stability data normalized by $\Delta\phi_{\mathrm{cr},a}$ and $\Delta\phi_{\mathrm{cr},b}$, respectively. This type of behavior is common when the critical wavenumber of the instabilities varies with the control parameters (e.g., Ref. 33).

We observe an increase in the number of Taylor–Görtler vortices present at onset in the unstable state as the Ekman number is reduced. In Fig. 6(a), the number of Taylor–

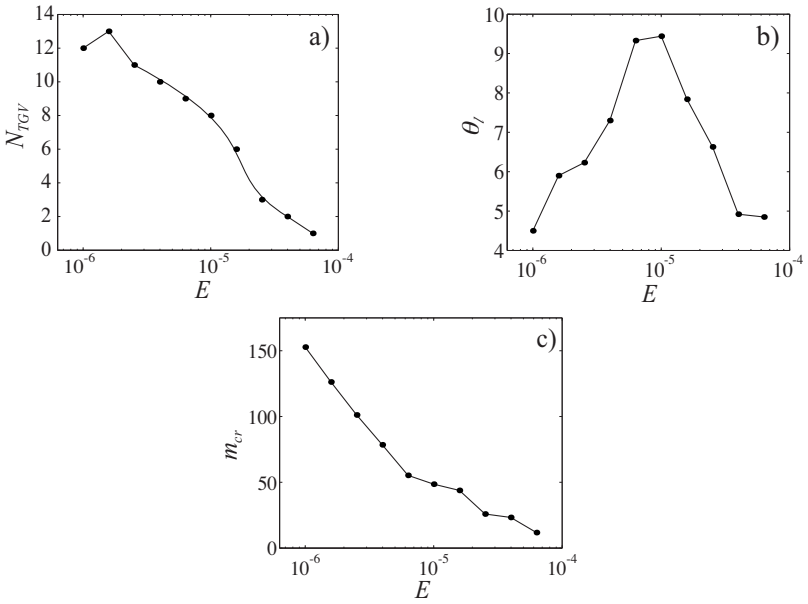

FIG. 6. (a) The number of Taylor–Görtler vortices, N_{TGV}, observed at onset as a function of Ekman number, E. (b) The latitudinal extent of the vortices, θ_l, in degrees. (c) The critical wavenumber, $m_{\mathrm{cr}}=(180/\pi)N_{\mathrm{TGV}}/\theta_l$, of the vortices.

Görtler vortices, N_{TGV}, is plotted versus the Ekman number. The individual vortices are identified by the presence of locally closed streamlines. As the instabilities are inherently transient, we have examined the properties of the instabilities at the instant when the outer shell is at its maximum retrograde position. However, the vortex count can also be performed on the time-averaged flow [e.g., Figs. 4(e) and 4(f)], which shows the same number of vortices.

To further quantify the instabilities, Fig. 6(b) shows the maximum latitudinal extent, θ_l, of the vortices when the outer boundary is at the maximum retrograde position. The critical wavenumber, $m_{\mathrm{cr}}=(180/\pi)N_{\mathrm{TGV}}/\theta_l$, is shown in Fig. 6(c); its value strongly increases with decreasing E. Numerical values of m_{cr} can be viewed as the number of vortices that would be present over an angular distance of 2π radians if the vortices were not spatially localized. The data shown in Fig. 6 demonstrate that the vortices become smaller and are generated closer to the equator as E is reduced. Although these results characterize the onset of Taylor–Görtler vortices, they suggest that the effect of centrifugal instabilities on the fluid volume becomes less pronounced at low Ekman numbers.

C. Zonal flows

Nontrivial time-averaged azimuthal velocities (i.e., zonal flows) are observed in all our numerical simulations. Figure 7 shows color plots of the typical structure of the zonal flow obtained from the numerical simulations for a stable case, and a case in which Taylor–Görtler vortices are present in the equatorial region. Underlying each of the color plots are time (i.e., $\bar{\cdot}$) and axially (i.e., $\langle\cdot\rangle$) averaged zonal velocities, $\langle\bar{w}\rangle$, plotted as a function of cylindrical radius, $s=r\sin\theta$. Plots of $\langle\bar{w}\rangle$ are referred to as geostrophic profiles. We see that in both the centrifugally stable [Figs. 7(a) and 7(c)] and unstable [Figs. 7(b) and 7(d)] cases, the zonal flow is characterized by predominantly retrograde motion in the interior, with a prograde jet in the outer equatorial region. For s

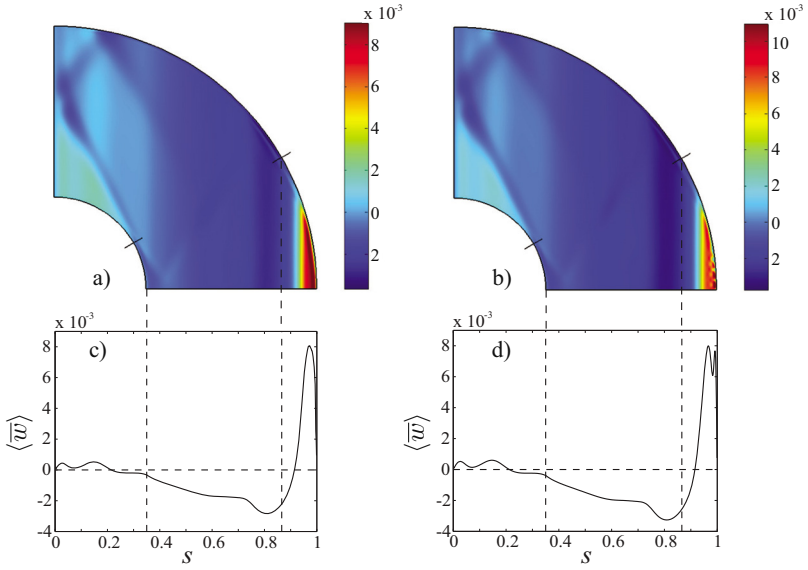

FIG. 7. (Color online) Comparison of zonal velocities between $E=10^{-5}$, $f=1$ cases that are centrifugally stable [(a) and (c)] $\epsilon=0.14$ and unstable [(b) and (d)] $\epsilon=0.15$. Panels (a) and (b) show the time-averaged zonal velocity in the meridional plane. Panels (c) and (d) show the corresponding geostrophic zonal velocities, $\langle\bar{w}\rangle$, as a function of cylindrical radius, s. The dashed vertical lines at $s=0.35$ and $s=0.87$ mark the radius of the inner sphere, $s=\eta$, and the critical latitude, s_{cr}, respectively.

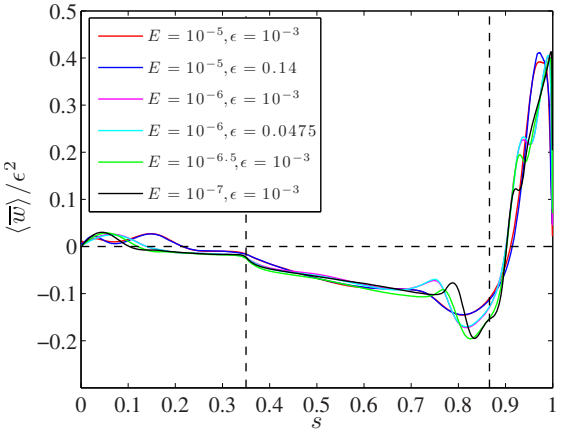

FIG. 8. (Color online) Geostrophic profiles for various E, ϵ, and $f=1$. The dashed vertical lines denote the radius of the inner sphere and critical latitude. All cases shown are centrifugally stable.

$\lesssim 0.35$, there is a weak mean flow with modulations that appear to correlate with the inertial wave structure. The zonal flow is retrograde and varies quasilinearly from $0.35 \lesssim s \lesssim 0.8$. The peak retrograde flow occurs at $s \approx 0.8$. At larger radii, the flow becomes prograde.

Comparison of the centrifugally stable and unstable cases shown in Figs. 7(c) and 7(d), respectively, allows us to infer the effects of the Taylor–Görtler vortices on the zonal flow. For the unstable case, there is a slight decrease in the magnitude of the prograde equatorial jet in the region where the vortices are present ($s \gtrsim 0.95$). The comparison of Figs. 7(c) and 7(d) shows that the Taylor–Görtler vortices do not drive the zonal flow; the general trends and magnitudes of the geostrophic profiles remain the same with and without the presence of the instabilities. Since they form primarily during the retrograde phase of the libration cycle, the net effect of the vortices is to locally exchange low angular momentum fluid between the boundary and the neighboring interior fluid. This causes the local decrease in zonal velocity at $s \gtrsim 0.95$.

Figure 8 plots geostrophic profiles from a variety of simulations in order to determine the effects of varying the libration amplitude and Ekman number on the zonal flow. All of the zonal velocities have been scaled by the square of the librational forcing, ϵ^2. The geostrophic profiles collapse well with this scaling, which is consistent with a nonlinear, Reynolds-stress driven mean flow (e.g., Refs. 9 and 21). Furthermore, this collapse implies that the primary properties of the zonal flow are independent of the Ekman number.

The most complex region in the geostrophic profiles is near s_{cr}, where the geostrophic shear layer associated with the critical latitude is predicted to develop (see Fig. 1). Noir *et al.*[11] proposed that the peak-to-peak amplitude of the shear scales as $E^{-3/10}$ over a width of $E^{1/5}$. This predicts that the geostrophic shear $d\langle \overline{w} \rangle / ds$ over this $E^{1/5}$ region will diverge as E becomes asymptotically small. However, in Fig. 8 it appears that this shear is beginning to saturate at $E \leq 10^{-6.5}$.

We have shown via Figs. 7(c) and 7(d) that the Taylor–Görtler vortices do not drive the zonal flows. Thus, there remain two nonlinear mechanisms through which libration can drive a zonal flow: (i) nonlinear self-interaction of inertial waves in the interior fluid and (ii) nonlinearities in the Ekman boundary layer present along the outer librating boundary. The contribution of each mechanism can be estimated by considering the time-averaged torque produced by the nonlinear forces acting on a cylinder coaxial with the rotation axis (e.g., see Refs. 9 and 19). Using equatorial and azimuthal symmetries and a cylindrical coordinate system (s, ϕ, z) in which the z-axis is aligned with the rotation axis, this torque can be written as

$$T = 4\pi s_c^2 \int_0^{h(s_c)} \overline{\mathrm{NL}} dz, \tag{23}$$

where $h(s_c) = \sqrt{r_o^2 - s_c^2}$ is the axial height of the cylinder, s_c is the radius of the cylinder, and $\overline{\mathrm{NL}}$ denotes the time-averaged nonlinear forces present in Eq. (8),

$$\overline{\mathrm{NL}} = \overline{u \frac{\partial w}{\partial r}} + \overline{\frac{v}{r} \frac{\partial w}{\partial \theta}} + \frac{\overline{uw}}{r} + \cot\theta \frac{\overline{vw}}{r}. \tag{24}$$

To elucidate the role of the interior stresses versus those acting within the Ekman layer, the torque in Eq. (23) can be decomposed as

$$T = T_{\mathrm{EBL}} + T_I, \tag{25}$$

where T_{EBL} and T_I are the torques in the Ekman boundary layer and in the fluid interior, respectively. We can make simple estimates for T based on the scalings of the inertial waves and of the Ekman boundary layers given in Fig. 1. Within the Ekman layers and away from the critical latitude, the velocity components scale as[6]

$$u \sim \mathcal{O}(\epsilon E^{1/2}); \quad v \sim \mathcal{O}(\epsilon); \quad w \sim \mathcal{O}(\epsilon). \tag{26}$$

Using these estimates, the dominant nonlinear terms in Eq. (23) scale as

$$\overline{u \frac{\partial w}{\partial r}}, \ \overline{\frac{v}{r} \frac{\partial w}{\partial \theta}}, \ \cot\theta \frac{\overline{vw}}{r} \sim \mathcal{O}(\epsilon^2), \tag{27}$$

where we have used $\partial / \partial r \sim \mathcal{O}(E^{-1/2})$.[6] Thus, integration of Eq. (23) across the Ekman layer gives

$$T_{\mathrm{EBL}} \sim \mathcal{O}(\epsilon^2 E^{1/2}). \tag{28}$$

In the fluid interior, nonlinear torques can be generated by the two shear layers spawned from the critical latitude on the inner and outer boundary (see Fig. 1). We denote these torques as $T_{I,i}$ and $T_{I,o}$, respectively. The shear layer generated on the inner sphere is characterized by a velocity scale of $E^{1/6}$ and a length scale $E^{1/3}$.[9] Employing these scalings, the dominant terms in Eq. (24) are

$$\overline{u \frac{\partial w}{\partial r}}, \ \overline{\frac{v}{r} \frac{\partial w}{\partial \theta}} \sim \mathcal{O}(\epsilon^2). \tag{29}$$

Integration across an $\mathcal{O}(E^{1/3})$ layer then gives

$$T_{I,i} \sim \mathcal{O}(\epsilon^2 E^{1/3}). \tag{30}$$

For the nonlinearities associated with the shear layers spawned from the outer sphere, we use the velocity scale of $E^{1/5}$ and length scale of $E^{1/5}$,[10] giving

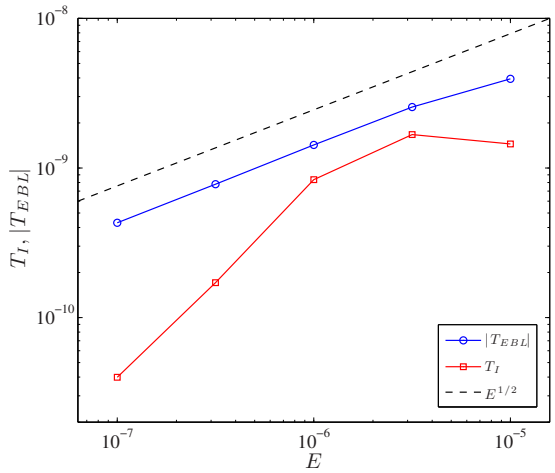

FIG. 9. (Color online) Nonlinear torques acting on a geostrophic cylinder of radius $s_c=0.675$ for $\epsilon=10^{-3}$ and $f=1$. T_{EBL} is the nonlinear torque within the Ekman boundary layer and T_I is the nonlinear torque acting within the bulk of the fluid outside of the Ekman layers. The dashed line represents the predicted torque scaling of $E^{1/2}$ for nonlinearities within the Ekman layer.

$$\overline{u\frac{\partial w}{\partial r}},\ \overline{\frac{v}{r}\frac{\partial w}{\partial \theta}} \sim \mathcal{O}(\epsilon^2 E^{1/5}). \tag{31}$$

Integrating across the $\mathcal{O}(E^{1/5})$ layer, we then have

$$T_{I,o} \sim \mathcal{O}(\epsilon^2 E^{2/5}). \tag{32}$$

Thus, the scalings given by Eqs. (28), (30), and (32) imply that

$$T_{\mathrm{EBL}}/T_{I,i} \sim \mathcal{O}(E^{1/6}), \quad T_{\mathrm{EBL}}/T_{I,o} \sim \mathcal{O}(E^{1/10}),$$
$$T_{I,o}/T_{I,i} \sim \mathcal{O}(E^{1/15}). \tag{33}$$

Thus, the torques produced by the inertial waves in the interior may dominate those in the Ekman layer, provided the constants of proportionality remain comparable. Note that these estimates ignore phase cancellations between the different velocity components that may occur in the shear layers (e.g., Ref. 9).

We have numerically evaluated Eq. (23) at the cylindrical midpoint, $s_c=0.675$, for $f=1$ over the range $E=10^{-5}-10^{-7}$ to test the torque scalings given above. The results of the calculations are shown in Fig. 9, where we have plotted $|T_{\mathrm{EBL}}|$ and $T_I=T_{I,i}+T_{I,o}$ with the $E^{1/2}$ scaling for comparison. The torque due to the nonlinear forces in the Ekman layer T_{EBL} remains negative for all E investigated and is larger in magnitude than the interior contribution T_I. Furthermore, T_{EBL} closely approximates the predicted $E^{1/2}$ slope given by Eq. (28). The interior torque T_I is positive for all E and does not appear to follow any simple scaling relationship over the Ekman numbers investigated. Thus, the scalings derived above for $T_{I,i}$ and $T_{I,o}$ are not valid within our parameter range. Because the difference $|T_{\mathrm{EBL}}|-T_I$ becomes larger as E is reduced from $10^{-5.5}$ to 10^{-7}, we argue that the zonal flow in our simulations is maintained by the nonlinearities present in the Ekman layer along the outer spherical boundary.

To further investigate the mechanism underlying the zonal flow generation, we compare a set of simulations at $E=10^{-5}$ and $\Delta\phi=10^{-3}$, with $f=1$ and $f=2.2$. At $f=2.2$, inertial waves are not excited in the fluid. Figures 10(a) and 10(b) show the nonlinear forces, $\overline{\mathrm{NL}}$, in the $f=1$ and $f=2.2$ simulations. The nonlinear forces are largest in the Ekman layers for both $f=1$ and $f=2.2$. For $f=1$, however, the nonlinearities in the interior remain finite, as can be seen in Fig. 10(a). (Note that we have saturated the color scheme for $f=1$ such that the interior nonlinear forces can be easily identified.) For $f=1$, the interior nonlinearities are largest along the shear layer emanating from the critical latitude on the inner sphere, as expected from the scalings given in Fig. 1. In Fig. 10(b), it can be seen that the interior nonlinear forces are close to zero when inertial waves are not excited.

Figures 10(c) and 10(d) show the normalized geostrophic profiles, $\langle\bar{w}\rangle/\epsilon^2$, for $f=1$ and $f=2.2$, respectively. In

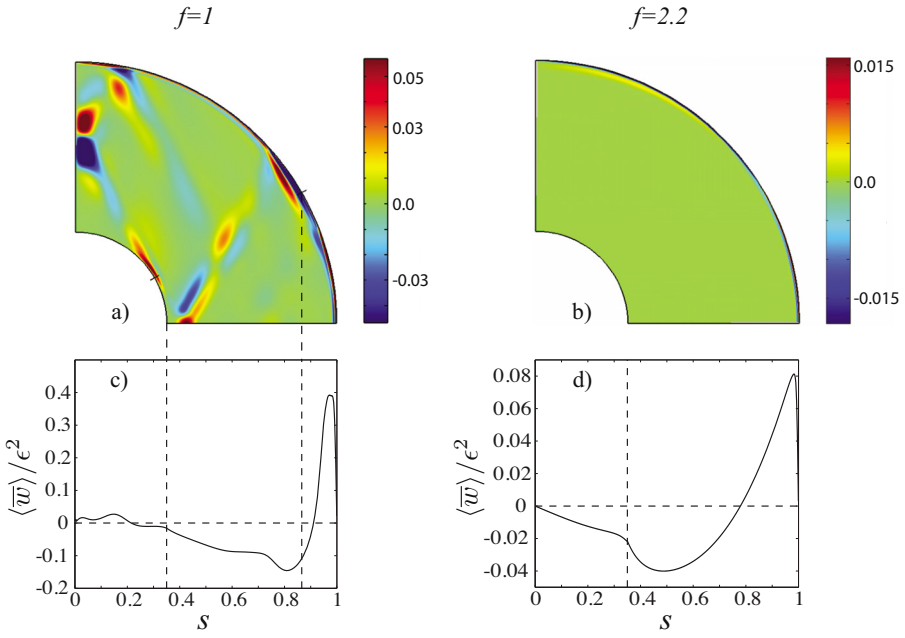

FIG. 10. (Color online) Time-average of the nonlinearities present in the azimuthal velocity equation, $\overline{\mathrm{NL}}$, for $E=10^{-5}$, $\Delta\phi=10^{-3}$, and (a) $f^*=1$, (b) $f^*=2.2$. Normalized geostrophic profiles for $E=10^{-5}$, $\Delta\phi=10^{-3}$, and (c), $f=1$, (d) $f=2.2$.

both cases we observe a retrograde zonal flow in the interior, flanked by an equatorial prograde jet. Thus the basic structure of the geostrophic profiles for $f>2$ (i.e., no inertial waves) are similar to cases with $f<2$ (i.e., including inertial waves). This implies that the basic geostrophic profile is generated by Ekman layer nonlinearities and not inertial waves. The differences in the shapes and amplitudes of the geostrophic velocities are likely due to the presence of the critical latitude in the $f=1$ case.

The geostrophic profiles change direction from retrograde in the interior to prograde at roughly $s\approx 0.8$ in our simulations and in the cylindrical laboratory experiments of Noir *et al.*[19] These results differ from the low frequency analytical predictions of Busse,[20] in which the zonal flow is retrograde throughout the fluid volume. The change in sign of our geostrophic profiles, shown in Figs. 8, 10(c), and 10(d), can be understood by considering a mass balance over the Ekman layer. During the prograde phase of a libration cycle, Ekman pumping acts to spin-up the interior by pulling fluid into the Ekman boundary layer at high latitudes and returning fluid to the interior at lower latitudes. Therefore, neglecting the effects of inertial waves in the boundary layer, the following condition holds during the prograde phase of libration:

$$\int_0^{2\pi}\int_0^{\theta_0} u_{\mathrm{in}}(r_E,\theta,t)\sin\,\theta d\theta d\phi = \int_0^{2\pi}\int_{\theta_0}^{\pi/2} u_{\mathrm{out}}(r_E,\theta,t)\sin\,\theta d\theta d\phi, \tag{34}$$

where r_E is the radial position within the Ekman layer and u_{in} and u_{out} represent the radial flow into and out of the Ekman layer, respectively. (An analogous expression holds during the retrograde phase of libration.) The angle, θ_0, is defined as the colatitude at which the radial velocity in the Ekman layer changes sign, i.e.,

$$u_{\mathrm{in}}(r_E,\theta_0,t)=u_{\mathrm{out}}(r_E,\theta_0,t)=0. \tag{35}$$

Our results show that the value θ_0 is approximately the same during both the prograde and retrograde phases. Thus, for the prograde phase, the radial velocity is predominantly positive for $\theta<\theta_0$ and negative for $\theta_0<\theta<\pi/2$. Assuming $u_{\mathrm{in}}\approx u_{\mathrm{out}}$ in Eq. (34), we find $\theta_0=60°$, which corresponds to $s\approx 0.87$. Since our results show that the sign of $\overline{\mathrm{NL}}$ is controlled by the radial velocity, we predict a change in sign of the geostrophic flow near θ_0. This θ_0 estimate is in qualitative agreement with the colatitude at which we observe a change in sign of the zonal flow in all of our geostrophic profiles. The above argument explains the existence of the prograde jet in the outer equatorial region, $s\gtrsim 0.8$.

IV. DISCUSSION

In this study we investigate the axisymmetric and equatorially symmetric response of a librationally driven fluid contained in a spherical shell of radius ratio $\eta=0.35$. The imposed symmetries of our model allow us to investigate Ekman numbers two orders of magnitude smaller than related studies.

Our results demonstrate that libration is capable of generating Taylor–Görtler vortices along the outer librating boundary during the retrograde phase of the libration cycle. This is in qualitative agreement with previous work.[12,15] In N09 it was argued that the formation of Taylor–Görtler vortices was controlled by a Reynolds number based on the thickness of the Ekman boundary layer, $\mathrm{Re}_{\mathrm{BL}}=\Delta\phi f E^{-1/2}$. We have tested this onset scaling down to $E=10^{-6}$ and find agreement within the uncertainties of our results. However, the calculated critical boundary layer Reynolds number, $\mathrm{Re}_{\mathrm{BL,cr}}$, for the onset of the vortices for various E was found to be 46, which is ~2.3 times larger than the value reported in the laboratory experiments of N09.

The zonal flows present in our simulations are largely axially invariant (geostrophic). They are characterized by retrograde flow throughout the interior ($s\lesssim 0.8$), with a stronger prograde jet in the equatorial region ($s\gtrsim 0.8$). By varying the libration amplitude and the Ekman number, our results demonstrate that the magnitude of the zonal flow scales as ϵ^2 and that the primary features of the flow are independent of E. Additionally, the onset of centrifugal instabilities has been shown to cause only a slight decrease in the magnitude of the prograde equatorial flow. Direct numerical evaluation of the nonlinear torques acting on a geostrophic cylinder has shown that the interior torques due to the nonlinearities in the internal shear layers are small in comparison to those present in the Ekman boundary layer. The interior nonlinear torque is found to decrease much more rapidly than that predicted by a simple scaling argument, suggesting phase cancellations between the velocity components are important in these regions (e.g., Ref. 9). Within our range of accessible E, simulations performed at $f>2$ (i.e., with no inertial waves present) produce zonal flows that are grossly similar to those at $f=1$ (i.e., with inertial waves present). Thus, we can conclude that the zonal flows in our simulations are driven predominantly by nonlinearities in the Ekman layer on the outer spherical shell boundary. The effects of centrifugal instabilities and inertial waves do not dominate the zonal flow generation process in our range of accessible parameters.

Recent $f\sim 1$ laboratory experiments[19] and a low f analytical study in a librating sphere[20] also found a predominantly retrograde zonal flow with ϵ^2 amplitude and E-independent behavior. In addition, the prograde flow near the outer librating boundary has also been found by Noir *et al.*[19] In contrast, Busse[20] predicted retrograde flow throughout the fluid interior for low libration frequencies. We find that conservation of mass requires there to be a change in sign of the radial velocity within the Ekman layer. This property leads to a change in sign of the nonlinear forces present within the Ekman layer, thus causing the observed change in sign of the zonal flow.

Estimates of $\mathrm{Re}_{\mathrm{BL}}$ for the librating planetary bodies of the Earth's moon, Mercury, Io, and Europa are 73, 490, 800, and 1300, respectively (see Table II of N09). Our results imply that these bodies are centrifugally unstable, giving respective supercriticalities, $\mathrm{Re}_{\mathrm{BL}}/\mathrm{Re}_{\mathrm{BL,cr}}$, of 1.6, 11, 17, and 28. However, at the lowest Ekman numbers accessible in our simulations, the instabilities at $\mathrm{Re}_{\mathrm{BL}}=\mathrm{Re}_{\mathrm{BL,cr}}$ are only generated close to the equator. Furthermore, these equatorially lo-

calized vortices do not strongly affect the mean zonal flows. Thus, our axisymmetric simulations suggest that near onset Taylor–Görtler vortices will not be of fundamental importance in planetary cores and subsurface oceans.

The dimensionless zonal velocities scale as $w \sim \epsilon^2$ in our simulations. This scaling allows us to provide estimates for W, the dimensional librationally driven zonal flow, of $W_M \sim 5 \times 10^{-9}$ m/s and $W_E \sim 10^{-7}$ m/s, for the planets Mercury and Europa, respectively. Here we have used the rotation rates and radii of Mercury and Europa, respectively, as $\Omega_{o,M} \approx 10^{-6}$ s^{-1} and $r_M \approx 2.4 \times 10^6$ m, and $\Omega_{o,E} \approx 2 \times 10^{-5}$ s^{-1} and $r_E \approx 1.6 \times 10^6$ m. The values for the librational forcing for each body are $\epsilon_M \approx 4/3 \times 10^{-4}$ and $\epsilon_E \approx 2 \times 10^{-4}$ (see Table II of N09). For comparison, estimates for the convectively driven flows that drive the dynamo in Earth's core are $W \sim 10^{-4}$ m/s.[34] Assuming the composition of Mercury's core is comparable to that of the Earth's iron rich outer core, we use a typical value of the magnetic diffusivity $\lambda \sim 1$ m^2/s to estimate a typical magnetic Reynolds number of $Rm = Wr_o/\lambda \sim \mathcal{O}(10^{-6})$. Since $Rm \ll 1$, this shows that viscous librational coupling alone will not induce significant planetary magnetic fields. Furthermore, we expect such flows to be incapable of generating observable secular variation.

We have shown that axisymmetric librationally driven zonal flows are small at planetary settings. However, it is possible that they can influence processes that occur on geological time-scales, such as the proposed tidally driven nonsynchronous rotation of Europa's ice shell (e.g., Refs. 35 and 36). Associated with the mean zonal flow is a small viscous torque that acts on the spherical shell boundaries. To accurately scale such mean torques to subsurface oceanic settings, future simulations will be carried out with realistic radius ratio values, $\eta \approx 0.90$.

ACKNOWLEDGMENTS

The authors wish to thank Fritz Busse for fruitful discussions and Bruce Bills and an anonymous reviewer for comments that significantly improved this manuscript. This work was supported by NASA Planetary Atmospheres Program Grant Nos. NNG06G197G and NNX09AE96G and by NASA Advanced Supercomputing Division Grant No. SMD-09-1274. Computational resources were also provided by the UCLA Hoffman2 cluster.

[1] R. L. Comstock and B. G. Bills, "A solar system survey of forced librations in longitude," J. Geophys. Res. **108**, 5100, doi:10.1029/2003JE002100 (2003).
[2] T. Van Hoolst, N. Rambaux, O. Karatekin, V. Dehant, and A. Rivoldini, "The librations, shape, and icy shell of Europa," Icarus **195**, 386 (2008).
[3] J. L. Margot, S. J. Peale, R. F. Jurgens, M. A. Slade, and I. V. Holin, "Large longitude libration of Mercury reveals a molten core," Science **316**, 710 (2007).
[4] P. H. Roberts, *The Encyclopedia of Solid Earth Geophysics* (van Nostrand Reinhold, New York, 1990).
[5] R. D. Lorenz, B. W. Stiles, R. L. Kirk, M. D. Allison, P. P. del Marmo, L. Less, J. I. Lunine, S. J. Ostro, and S. Hensley, "Titan's rotation reveals an internal ocean and changing zonal winds," Science **319**, 1649 (2008).
[6] H. P. Greenspan, *The Theory of Rotating Fluids* (Cambridge University Press, London, 1968).
[7] L. Messio, C. Morize, M. Rabaud, and F. Moisy, "Experimental observation using particle image velocimetry of inertial waves in a rotating fluid," Exp. Fluids **44**, 519 (2008).
[8] J. Noir, D. Brito, K. D. Aldridge, and P. Cardin, "Experimental evidence of inertial waves in a precessing spheriodal cavity," Geophys. Res. Lett. **28**, 3785, doi:10.1029/2001GL012956 (2001).
[9] R. R. Kerswell, "On the internal shear layers spawned by the critical regions in oscillatory Ekman boundary layers," J. Fluid Mech. **298**, 311 (1995).
[10] P. H. Roberts and K. Stewartson, "On the stability of a Maclaurin spheriod of small viscosity," Astron. J. **137**, 777 (1963).
[11] J. Noir, D. Jault, and P. Cardin, "Numerical study of the motions within a slowly precessing sphere at low Ekman number," J. Fluid Mech. **437**, 283 (2001).
[12] K. D. Aldridge, "An experimental study of axisymmetric inertial oscillations of a rotating sphere," Ph.D. thesis, Massachusetts Institute of Technology, Cambridge, Massachusetts, 1967.
[13] K. D. Aldridge and A. Toomre, "Axisymmetric inertial oscillations of a fluid in a rotating spherical container," J. Fluid Mech. **37**, 307 (1969).
[14] A. Tilgner, "Driven inertial oscillations in spherical shells," Phys. Rev. E **59**, 1789 (1999).
[15] J. Noir, F. Hemmerlin, J. Wicht, S. M. Baca, and J. M. Aurnou, "Laboratory models of librationally-driven flow in planetary cores and sub-surface oceans," Phys. Earth Planet. Inter. **173**, 141 (2009).
[16] J. Aubert, S. Jung, and H. L. Swinney, "Observations of zonal flow created by potential vorticity mixing in a rotating fluid," Geophys. Res. Lett. **29**, 1876, doi:10.1029/2002GL015422 (2002).
[17] M. H. Heimpel and J. M. Aurnou, "Turbulent convection in rapidly rotating spherical shells: A model for equatorial and high latitude jets on Jupiter and Saturn," Icarus **187**, 540 (2007).
[18] A. Tilgner, "Zonal wind driven by inertial modes," Phys. Rev. Lett. **99**, 194501 (2007).
[19] J. Noir, M. A. Calkins, M. Lasbleis, J. Cantwell, and J. M. Aurnou, "Experimental study of libration-driven zonal flows in a straight cylinder," Phys. Earth Planet. Inter. (in press).
[20] F. H. Busse, "Mean zonal flows generated by librations of a rotating spherical cavity," J. Fluid Mech. **650**, 505 (2010).
[21] F. H. Busse, "Steady fluid flow in a precessing spheroidal shell," J. Fluid Mech. **33**, 739 (1968).
[22] S. C. R. Dennis and J. D. A. Walker, "Calculation of the steady flow past a sphere at low and moderate Reynolds numbers," J. Fluid Mech. **48**, 771 (1971).
[23] R. Peyret, *Spectral Methods for Incompressible Viscous Flow* (Springer-Verlag, New York, 2002), Vol. 148.
[24] P. Marcus and L. S. Tuckerman, "Simulation of flow between concentric rotating spheres. Part 1. Steady states," J. Fluid Mech. **185**, 1 (1987).
[25] W. Ni and N. J. Nigro, "Finite element analysis of the axially symmetric motion of an incompressible viscous fluid in a spherical annulus," Int. J. Numer. Methods Fluids **19**, 207 (1994).
[26] M. Rieutord, "Inertial modes in the liquid core of the Earth," Phys. Earth Planet. Inter. **91**, 41 (1995).
[27] M. Rieutord and L. Valdettaro, "Inertial waves in a rotating spherical shell," J. Fluid Mech. **341**, 77 (1997).
[28] P. Marcus and L. S. Tuckerman, "Simulation of flow between concentric rotating spheres. Part 2. Transitions," J. Fluid Mech. **185**, 31 (1987).
[29] K. Nakabayashi, "Transition of Taylor–Görtler vortex flow in spherical Couette flow," J. Fluid Mech. **132**, 209 (1983).
[30] C. D. Andereck, S. S. Liu, and H. L. Swinney, "Flow regimes in a circular Couette system with independently rotating cylinders," J. Fluid Mech. **164**, 155 (1986).
[31] P. G. Drazin and W. H. Reid, *Hydrodynamic Stability* (Cambridge University Press, Cambridge, 2004).
[32] W. S. Saric, "Görtler vortices," Annu. Rev. Fluid Mech. **26**, 379 (1994).

[33]P. J. Blennerhassett and A. P. Bassom, "The linear stability of high-frequency flow in a torsionally oscillating cylinder," J. Fluid Mech. **576**, 491 (2007).
[34]D. Gubbins and P. H. Roberts, *Geomagnetism* (Academic, Orlando, 1987), Vol. 2.
[35]P. E. Geissler, R. Greenberg, G. Hoppa, P. Helfenstein, A. McEwen, R. Pappalardo, R. Tufts, M. Ockert-Bell, R. Sullivan, R. Greeley, M. J. S. Belton, T. Denk, B. Clark, J. Burns, J. Veverka, and Galileo Imaging Team, "Evidence for non-synchronous rotation of Europa," Nature (London) **391**, 368 (1998).
[36]S. A. Kattenhorn, "Nonsynchronous rotation evidence and fracture history in the bright plains region, Europa," Icarus **157**, 490 (2002).